FEATURE ARTICLE

Molecular Structure and Orientation: Concepts from Femtosecond Dynamics

J. Spencer Baskin and Ahmed H. Zewail*

Arthur Amos Noyes Laboratory of Chemical Physics, California Institute of Technology, Pasadena California 91125

Received: December 18, 2000; In Final Form: February 7, 2001

In this article, we are concerned with the basic concepts of molecular orientation, its dynamics on the femtosecond and picosecond time scales, and the direct relationship of the foregoing to determination of molecular structures. Our aim is to present a unified picture for the dynamics in different phases: coherent inertial in isolated molecules, partially coherent in dense fluids, and reaching the diffusive limit in liquids. We compare theory and experiment for reactive and nonreactive systems, with examples of studies from this laboratory in molecular beams, dense fluids, liquids, proteins, and micelles. We discuss the high precision achieved in molecular structural determination for large isolated molecules. Important to molecular orientation in space is the time scale, and we present here the two limits: quantum-state orientation (long time or continuous wave experiment) and classical-like orientation achieved with femtosecond resolution.

I. Introduction

The fact that molecules have well-defined structures is a concept of fundamental importance in chemistry.[1] A corollary to this idea is the fact that profound consequences of spatial *orientation* of molecules are ubiquitous in all areas of molecular science. Chemical and many physical and biological properties of molecules are inherently orientation-dependent, and therefore the degree of orientation and the evolution of orientation significantly affect studies of molecular systems in all physical phases, from dilute gases to solids. The type of orientational motion encountered varies from generally negligible in solids, to diffusive in liquids, to hindered in dense gases, to purely inertial and coherent in isolated molecules.

Hydrodynamic descriptions of rotational diffusion in liquids have a long history,[2,3] and the time scales of diffusive reorientation have been amenable to direct studies for many decades.[4] The consequences of free (inertial) rotational motion of molecules began to receive attention in the 1960s.[5,6] With the development of femtosecond laser techniques, experimental investigations have now spanned the full range of time scales and environments of molecular orientational motion.[7]

This article is concerned with some basic concepts of molecular orientational dynamics, with an emphasis on its role in femtosecond studies and its relationship to molecular structures. The femtosecond time scale is unique in that the orientation of molecular samples, even when undergoing free rotation, can be followed as it evolves, providing direct information on the nature of the motion and the forces that govern it. The topics that will be addressed are the following: free rotational motion of isolated molecules; orientation in the presence of collisions and the effect of solvent density in bridging the gap from inertial to diffusive motion, spanning gases and liquids; and orientation in reactions. We conclude with a description of molecular orientation in space and time, connecting the regimes of short- and long-time or continuous wave (cw) experiments. Some aspects of the basic experimental implementation of the measurements are also discussed.

II. Orientation of Free Molecules

When an isotropic sample is excited by a linearly polarized pump pulse (polarization vector $\vec{\epsilon}_1$) via an electric-dipole allowed vibronic transition, there is created at the instant of excitation ($t = 0$) a spatial alignment or orientational anisotropy of the excited state population (Figure 1), because the probability for absorption is dependent upon the relative orientation of $\vec{\epsilon}_1$ and the molecular transition dipole vector $\vec{\mu}_1$. The excited ensemble is created with its transition dipoles exhibiting a cosine-squared distribution around $\vec{\epsilon}_1$ (Figure 1, bottom). Subsequent rotational motion causes an evolution of that distribution, as represented schematically by snapshots after $t = 0$ at the top of Figure 1, and the evolving dipole distribution at the bottom, for the case of a simple rotor. (Recurrences in the ensemble orientation at specific times are a quantum phenomenon and will be discussed later in this section.)

The preceding paragraph adopts a fundamentally classical viewpoint in describing the phenomenon of molecular orientation. As this viewpoint provides an almost entirely adequate basis for understanding and discussing femtosecond experiments, it will be relied upon heavily in this work. A brief discussion of the quantum origins of orientational dynamics and the differences to be expected between experiments using femtosecond pulses and those using nanosecond or longer pulses (cw excitation) will be given in section VI.

To investigate the nature of molecular orientation, we typically proceed experimentally by the measurement of the macroscopic transient polarization anisotropy, $r(t)$. Following the excitation process, the sample is interrogated by interaction with a time-delayed linearly polarized probe pulse using any of a variety of detection schemes chosen to produce a signal proportional to the total population that undergoes the probe

10.1021/jp004525p CCC: $20.00
Published on Web 03/27/2001

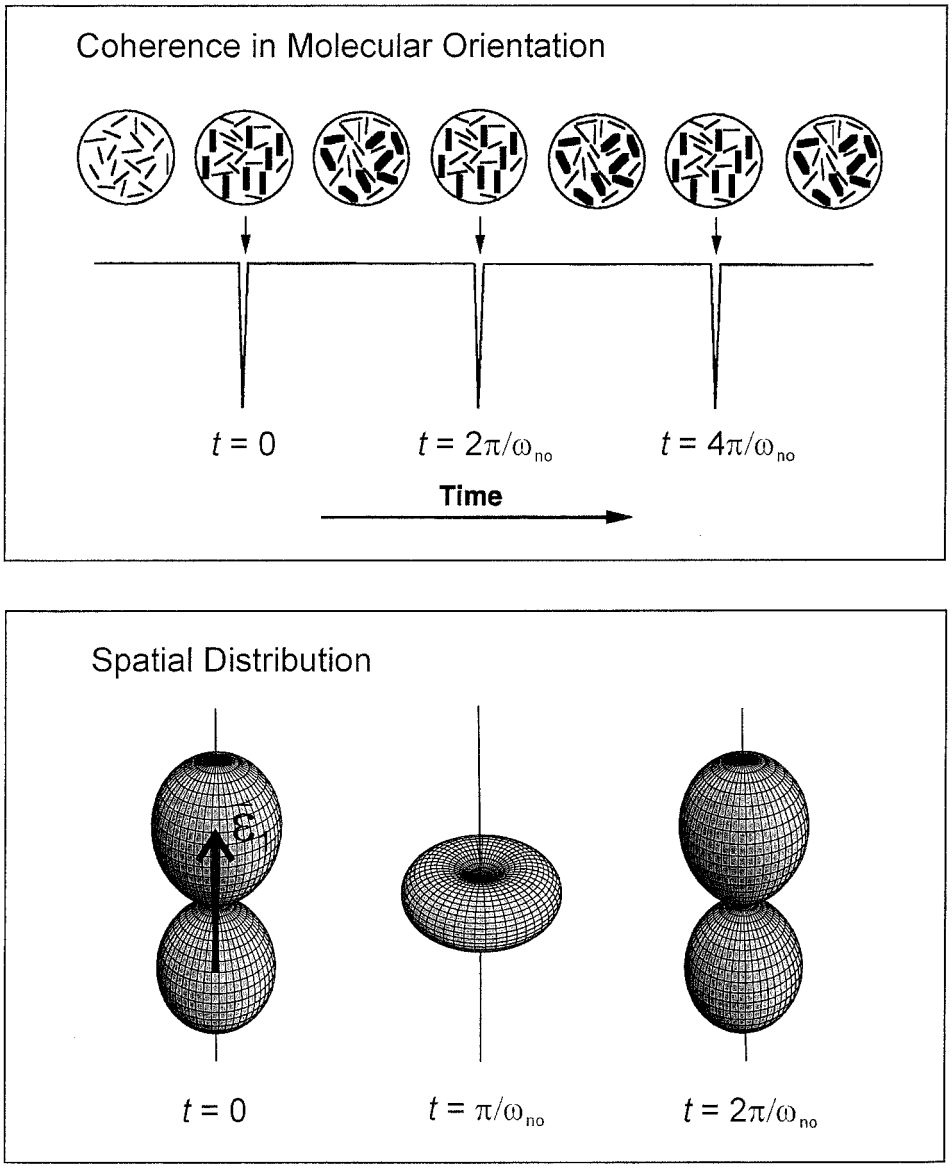

Figure 1. (Top) General concept of time-resolved orientation experiments on isolated molecules. An isotropic distribution of dipoles is excited at $t = 0$ by a vertically polarized light pulse. The thicker lines represent dipoles in their excited states, which follow individual rotational trajectories. (Bottom) Spatial distributions of transition dipole orientations for the excited state population at selected times are shown. The distributions are axially symmetric about the pump polarization vector $\vec{\epsilon}_1$.

transition. The experimental quantity is

$$r(t) = (S_{\parallel}(t) - S_{\perp}(t))/(S_{\parallel}(t) + 2S_{\perp}(t)) \quad (1)$$

where $S_{\parallel}(t)$ and $S_{\perp}(t)$ are the transient pump−probe signal intensities measured for probe polarization vector parallel and perpendicular, respectively, to that of the pump. This quantity is equal to the time correlation function of the transition dipole unit vectors (see, e.g., ref 8):

$$r(t) = 0.4\langle P_2[\hat{\mu}_1(0)\cdot\hat{\mu}_2(t)]\rangle \quad (2)$$

where $\vec{\mu}_2$ is the probe-transition dipole vector; $\hat{\mu}_i = \vec{\mu}_i/|\vec{\mu}_i|$; $P_2(x) = 0.5(3x^2 - 1)$ is the second-order Legendre polynomial; and the angle brackets denote a weighted average over the rotational state distribution of molecules in the sample.

The real-time observation of the femtosecond to picosecond evolution of the anisotropy of molecular samples has been exploited for almost two decades in the study of isolated molecules. A principal motivation for such studies is the valuable information about molecular structures that derives from the observation of coherent orientational motion of molecules, resulting in rotational recurrences directly seen in $r(t)$. (For reviews, see refs 7 and 9.) The decay of the anisotropy at short times has also been observed in isolated molecules (see, e.g., refs 10−13), and this behavior serves as a fundamental probe of *inertial* motion at finite temperature in a manner analogous to the role it has long played in studies of *diffusive* reorientation in liquids. Both classical and quantum mechanical theoretical treatments based on free rigid rotor motion (see, e.g., refs 6 and 14) have been very successful at describing the decay, and the recurrences.[14,15]

Here we summarize some essential characteristics of molecular orientation dynamics for symmetric top molecules undergoing classical free rotation. The motion of a rigid symmetric rotor is describable[16] as a combination of two independent motions (Figure 2, inset): nutation of the top's symmetry or figure axis about the angular momentum vector $\vec{j}$ at angular frequency ω_n, and rotation about the figure axis at angular frequency ω_r. Using the standard definition of rotational constant in frequency units,

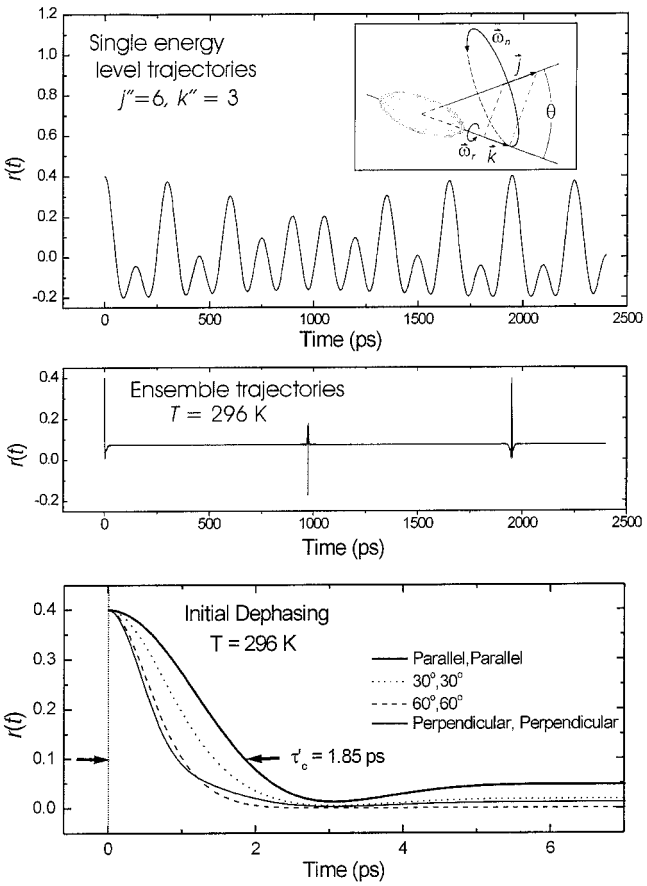

Figure 2. (Top) Theoretical anisotropy for a single energy level of a symmetric top with $B_{\|} = 2.603$ GHz and $B_{\perp} = 0.2566$ GHz and (||,||) transition dipoles. Inset: Classical motion of a rigid symmetric top molecule. $\vec{j}$ is the total angular momentum vector and $\vec{k}$ is its projection along the figure axis. ω_n and ω_r are the angular frequencies of nutation about $\vec{j}$ and rotation about the figure axis, respectively. (Middle) Theoretical anisotropy for a thermal sample of the same molecule at $T = 296$ K. (Bottom) Expanded view of the early time anisotropy decays of the same molecule, again at $T = 296$ K, but now for various dipole directions as indicated.

$B_i = \hbar/(4\pi I_i)$, where I_i is the moment of inertia about the ith principal inertial axis, the angular frequencies are given classically[16] by $\omega_n = 4\pi B_{\perp} j = \omega_{no} j$, and $\omega_r = 4\pi(B_{\|} - B_{\perp}) j \cos\theta = \omega_{ro} k$. Here, $B_{\|}$ and $B_{\perp}$ are the excited-state rotational constants of the molecule about its figure axis and about any axis perpendicular to it, respectively, $\omega_{no} = 4\pi B_{\perp}$, $\omega_{ro} = 4\pi(B_{\|} - B_{\perp})$, and $k = j \cos\theta$. Introduction of the quantity $\hbar$ in the definition of B requires that the values j and k that appear in the classical frequency expressions given above be the magnitudes divided by $\hbar$ of, respectively, the classical total angular momentum $\vec{j}$ and of its axial component $\vec{k}$; i.e., $j = |\vec{j}|/\hbar$ and $k = |\vec{k}|/\hbar$. Thus, ω_{no} and ω_{ro}, referred to as the fundamental angular frequencies of nutation and rotation, correspond to $|\vec{j}| = \hbar$ and $|\vec{k}| = \hbar$, respectively.

A broadly applicable prescription for calculation of $r(t)$ for this idealized case, which, nonetheless, provides a useful approximation to the motion of many real molecules, is given in the Appendix in terms of the Euler angles θ, φ, and ψ relating the principal inertial axes (x, y, z) of the molecule to space fixed axes (see Figure 12). It is found that the state-resolved anisotropy may be a function not only of time but also of j (through the frequencies), θ (both explicitly and through ω_r), and ψ_0, the initial rotational phase angle, which has no influence on rotational energy. We consider here two simple but common cases: $\hat{\mu}_1$ and $\hat{\mu}_2$ both either parallel or perpendicular to the figure axis of the molecule. The relation of the two transition moments to the figure axis is designated by the notations (||,||) and ($\perp$,$\perp$), respectively. In the first case, application of eq A-4 with $\hat{\mu}_1 = \hat{z}(0)$ and $\hat{\mu}_2 = \hat{z}(t)$ yields

$$r_{\|,\|}(j,\theta,t) = {}^1/_{10}(3\cos^2\theta - 1)^2 + {}^6/_5 \sin^2\theta \cos^2\theta \cos(j\omega_{no}t) + {}^3/_{10}\sin^4\theta \cos(2j\omega_{no}t) \quad (3)$$

Because rotation about the figure axis is not reflected in the motion of a parallel dipole, $r_{\|,\|}$ does not depend on the rotation frequency ω_r, nor was integration over ψ_0 (eq A-3) required.

Equation 3 is seen to be periodic in time with a period of $2\pi/\omega_n = 1/(2B_{\perp}j)$, independent of θ. A rigorous treatment shows that the quantum mechanically correct behavior requires the term periodic in frequency $\omega_n = j\omega_{no}$ be replaced by an average of terms in $j\omega_{no}$ and $(j + 1)\omega_{no}$ and that the frequency $2\omega_n$ be replaced by $(2j + 1)\omega_{no}$. The largest common factor of these three frequencies is simply ω_{no}, so $r_{\|,\|}(j,\theta,t)$ is, in general, strictly periodic only at the fundamental rotational period, $1/(2B_{\perp})$, regardless of the value of j. The initial anisotropy is equal to 0.4, as is always the case when the pump and probe dipoles have the same orientation in the molecule-fixed frame. Figure 2 shows a calculation using eq 3 (with corrected frequencies) for $j = 6$ and $k = 3$ when $2\pi/\omega_{no} = 1948$ ps. (The rotational constants used are approximately those of S_1 *trans*-stilbene.)[17]

A situation of particular interest and simplicity is that of j perpendicular to the figure axis, which holds to good approximation for all linear molecules. With $\theta = \pi/2$ and $(2j + 1)\omega_{no}$ replacing $2j\omega_{no}$, eq 3 reduces to

$$r_{\|,\|}(j,\pi/2,t) = 0.1 + 0.3\cos[((2j + 1)\omega_{no}t)] \quad (4)$$

which oscillates at $(2j + 1)$ times the fundamental angular frequency and has a mean value of 0.1. (In this case, nutation and rotation are interchangeable terms, since there is no rotation about the figure axis.)

For the ($\perp$,$\perp$) dipole case, taking, for example, $\hat{\mu}_1 = \hat{x}(0)$ and $\hat{\mu}_2 = \hat{x}(t)$, one obtains from eq A-4

$$r_{\perp,\perp}(j,\theta,t) = {}^1/_{40}(3\cos^2\theta - 1)^2 + {}^3/_{10}\cos^2\theta \sin^2\theta \cos(j\omega_{no}t) + {}^3/_{40}\sin^4\theta \cos(2j\omega_{no}t) + {}^9/_{80}\sin^4\theta \cos(2k\omega_{ro}t) + {}^3/_{40}(1 + \cos\theta)^2 \sin^2\theta \cos((j\omega_{no} + 2k\omega_{ro})t) + {}^3/_{40}(1 - \cos\theta)^2 \sin^2\theta \cos((j\omega_{no} - 2k\omega_{ro})t) + {}^3/_{160}(1 + \cos\theta)^4 \cos(2(j\omega_{no} + k\omega_{ro})t) + {}^3/_{160}(1 - \cos\theta)^4 \times \cos(2(j\omega_{no} - k\omega_{ro})t) \quad (5)$$

where the quantum frequency corrections are omitted for simplicity. Both nutation and rotation about the figure axis influence this expression. Rotation enters only in the form of the overtone $2\omega_r$ because positions of a perpendicular dipole that are separated by a π radian rotation are optically equivalent. The dependence of $r_{\perp,\perp}(j,\theta,t)$ on two independent fundamental frequencies means that this anisotropy generally displays no strict periodicity as does $r_{\|,\|}(j,\theta,t)$.

Given an expression for $r(j,\theta,t)$ for each rotational energy level, the macroscopic (and hence experimentally observable) anisotropy will depend on the weight accorded to each in the ensemble average of eq 2. As an example of the simplest case, the observation of a single-energy-level anisotropy has been demonstrated for Li_2 by first using a narrow bandwidth cw laser to populate a selected excited rovibronic level (well above

thermal energies), then performing a femtosecond pump−probe experiment on that population.[18] The result is a purely cosinusoidally modulated signal represented to first order (neglecting centrifugal distortion) by eq 4. The measured period and knowledge of the value of j allows the structural constant $B_\perp$ to be determined.

More generally, a thermal population is probed, and then a large number of different single-energy-level signals modulated by different frequencies are observed together (incoherently). An example of an anisotropy from such a thermal distribution is shown in the middle of Figure 2 for the same molecule as used for the energy-resolved calculation at the top of the figure. At early time, the superposition of numerous cosinusoidal signals leads to a dephasing of the initial alignment, resulting in a decay of the anisotropy. The dephasing rate depends on the rotational constants, the dipole direction, and the rotational temperature. At the bottom of Figure 2 are shown examples of the initial anisotropy decay as calculated for a room-temperature rotational population distribution, again with rotational constants approximating those of S_1 *trans*-stilbene.

Precise expressions can be derived[8,19] for the characteristic dephasing time of an ensemble of linear molecules in the (||,||) dipole case (eq 4); the coherence time, τ'_c, defined as the time for the anisotropy to fall to 0.1, is given by

$$\tau'_c = 2.942(TB_\perp)^{-1/2}\ \text{ps} \qquad (6)$$

where T is the temperature in degrees Kelvin and $B_\perp$ is expressed in cm^{-1}. This expression is found to hold to high accuracy for the (||,||) dipole case of prolate nonlinear symmetric tops also (eq 3), an example being the case shown in Figure 2. Note that eq 6 is derived by assuming that the bandwidths of the pump and probe pulses span with equal spectral densities all allowed transitions from all populated rotational levels of the relevant initial vibronic state. When this is not the case, the time dependence will be a function also of the overlap of the pulse spectra with the rotational contour of the transition.

Observation of the dephasing described above and shown in Figure 2 requires only that the collision time in a thermal sample of molecules is long compared to the rotation time (typically a few picoseconds). When the collision interval is much longer, as in molecular beam studies, the possibility exists for complete or partial *rephasing*, or recurrence, of the macroscopic alignment. Rephasing will occur when the nutation and rotation periods of a significant fraction of the molecules are commensurable (i.e., have a common multiple), or nearly so. Such is clearly the case for rigid symmetric tops, for which the nutation and rotation frequencies are integral (based on the quantization of j and $j\cos\theta \equiv k$) multiples of the fundamental frequencies, ω_{no} and ω_{ro}. In the (||,||) dipole case, complete rephasing occurs at times $m(2\pi/\omega_{no})$ for integer m, with a partial negative recurrence at times $(m + {}^1/_2)(2\pi/\omega_{no})$ (see Figure 2, middle).

In the (⊥,⊥) dipole case, there are terms periodic in the angular frequencies $\omega_1 = \omega_{no}$ and $\omega_2 = 2\omega_{ro}$ contributed by molecules of all energy levels (see eq 5). In addition, from those levels with $k \sim j$ there are terms quasiperiodic in $\omega_3 = \omega_{no} + 2\omega_{ro}$ and $\omega_4 = 2(\omega_{no} + \omega_{ro})$ (including consideration of the above-specified quantum corrections to ω_n and $2\omega_n$). Note that, since $\cos\theta = k/j$, the apparent contributions of the $k \sim j$ levels at the difference frequencies, $\omega_{no} - 2\omega_{ro}$ and $2(\omega_{no} - \omega_{ro})$, have negligible amplitude. Thus, partial recurrences appear in $r_{\perp,\perp}(t)$ at times $m{\cdot}T$, where m is an integer and $T = 2\pi/\omega_i$, for $i = 1-4$. These times are directly related to the structural parameters $B_\perp$ and $B_\parallel$, and recurrence measurement therefore provides information about the molecule's structure.

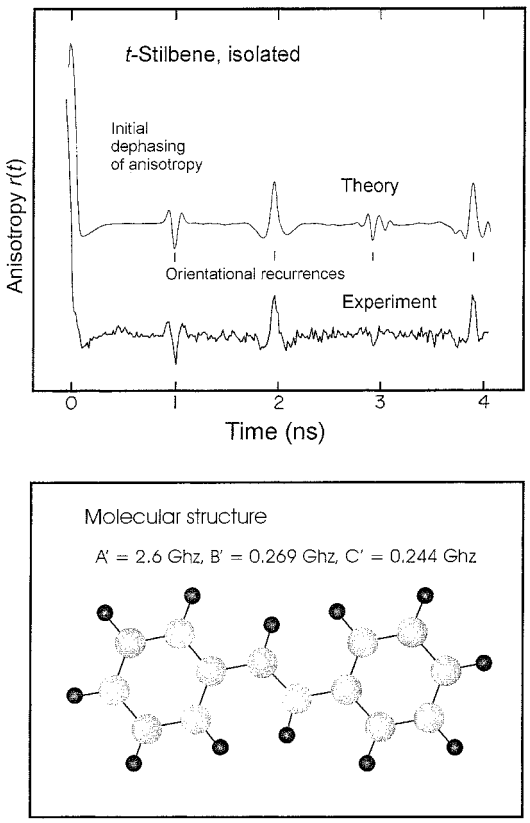

Figure 3. Comparison of experimental and theoretical anisotropies of jet-cooled samples of *trans*-stilbene (from ref 15) and the structure deduced from rotational coherence measurements.[17]

The nature of rotational coherence recurrences and their dependence on molecular structure and dipole directions have been described in detail elsewhere,[17,20] and fully quantum mechanical calculations can be shown to give virtually identical results to those obtained by use of the expressions presented here. Experimental application has also been extensive and has proven rotational coherence spectroscopy to be a powerful, Doppler-free, technique for the determination of molecular structure, and notably, that it is broadly applicable to real molecules, not just the rigid symmetric tops considered here; more than one hundred structures have been studied by rotational coherence spectroscopy (RCS) in laboratories around the world. As an example, a fluorescence anisotropy measurement of jet-cooled *trans*-stilbene is shown in Figure 3, plotted with a quantum-theoretical asymmetric-top simulation with appropriately chosen rotational constants. The molecular structure deduced with the aid of such measurements[17] is also shown.

III. Inertial to Diffusive Motion: Effect of Solvent Density

With an increase in the frequency of $\vec{j}$-changing collisions suffered by the molecules under study, the coherent and inertial rotational motion described in the preceding section survives for shorter and shorter times. At the molecular level, the situation for rotational dynamics is represented schematically in Figure 4, where the rotation of a diatomic solute molecule in a bath of solvent particles is controlled by the rate of collisions and by the effectiveness of those collisions in transferring angular momentum to or from the solute.[13] At gas-phase densities, changes in the recurrences can be monitored for obtaining

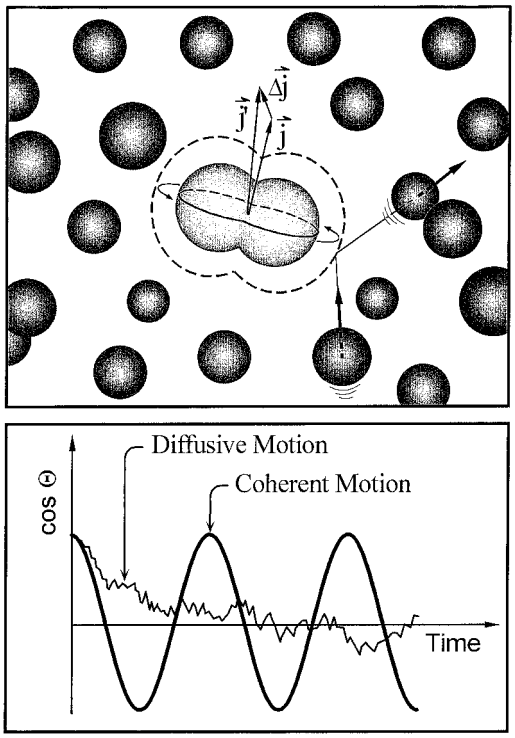

Figure 4. (Top) Schematic of the microscopic origin of friction on the rotational motion of a diatomic solute in atomic solvent. A random collision interrupts the free rotation of the diatom and causes a change $\Delta\vec{j}$ in angular momentum (from initial $\vec{j}$ to final $\vec{j}'$). (Bottom) The limiting cases of diffusive and purely coherent rotation are illustrated conceptually by a plot of $\cos(\Theta(t))$, where $\Theta(t)$ is the evolution with time of the polar angle formed by the diatom internuclear axis with its direction at $t = 0$.

information about the collision dynamics.[21] At even moderate densities (a few atoms/nm^3), collisions in molecular fluids occur at subpicosecond intervals.

With femtosecond time resolution, the rotational evolution of the solute can be precisely observed, and its dependence on solvent properties and densities can be characterized.[13] Such measurements probe directly the nature of microscopic friction, the interaction of solvent and solute at the molecular level, which plays a fundamental role in the dynamic evolution of solution phase chemical and physical processes.

Theoretical models of the role of friction in controlling molecular rotation have a long history (see, e.g., refs 2−6 and 22). The reorientational motion of a solute molecule in high-density fluids may be treated as a form of rotational Brownian motion. Focusing on the motion of a linear rotor with two rotational degrees of freedom, the total torque acting on the molecule is separated into the frictional torque, $-\xi I\vec{\omega}$, which is proportional to and opposes the angular velocity $\vec{\omega}$, and a random torque $\vec{T}$. Here, I is the unique moment of inertia of the rotor and ξ is the reduced rotational friction coefficient. A Langevin equation treatment,[23] $I(\partial/\partial t)\vec{\omega}(t) = -\xi I\vec{\omega}(t) + \vec{T}$, leads to an exponential decay of the angular velocity autocorrelation function ($\Omega(t) = \langle\vec{\omega}(t)\cdot\vec{\omega}(0)\rangle$) with a decay rate of ξ, and to the following analytical expression for transient anisotropy,

$$r(t) = 0.4\exp\left(-\frac{6kT}{I}(\tau^2 e^{-t/\tau} + \tau t - \tau^2)\right) \qquad (7)$$

where $\tau = 1/\xi$. This gives the correct inertial limit at early time:

$$r(t) = 0.4\exp\left(-\frac{3kT}{I}t^2\right) \qquad (8)$$

and an exponential decay for $t \gg \tau$,

$$r(t) \propto \exp(-6D_r t) \qquad (9)$$

using the Langevin−Einstein value for the rotational diffusion constant, $D_r = kT/(\xi I) = kT\tau/I$, which is the well-known result for the diffusive limit. This treatment is invalid under conditions of large angle free (inertial) rotation, however, and therefore is not useful under low friction conditions.

To apply the above expressions, a value of ξ is required. Hydrodynamic theory allows one to calculate ξ for an idealized ellipsoidal solute in a viscous fluid continuum as a function of the ellipsoid dimensions, shear viscosity η of the solvent, and the boundary condition assumed at the solute−solvent interface.[3,24] This treatment is valid in the same limit as the Langevin treatment; that is, for small solvent/solute mass ratio and collision time short on the time scale of free rotation, and the choice of boundary condition appropriate to a particular system remains a source of uncertainty in the result.

For example, for a prolate ellipsoid of revolution about an axis perpendicular to the symmetry axis, which is the case appropriate to the anisotropy of a diatom with transition dipole parallel to the internuclear axis, ξ for sticking boundary condition is given by[3]

$$\xi_{stick} = \frac{4\eta V}{I}\frac{1-\beta^4}{\frac{(2\beta^2-\beta^4)}{\sqrt{1-\beta^2}}\ln\left[{}^1/_\beta(1+\sqrt{1-\beta^2})\right]-\beta^2} \qquad (10)$$

where the ellipsoid has semimajor axis a and semiminor axis b, V is the ellipsoid volume ($V = {}^4/_3\pi ab^2$), and $\beta = b/a$. The ratio ξ_{slip}/ξ_{stick} may then be found in Table 1 of ref 24 as a function of b/a.

Defining τ_{rot} as the time constant of anisotropy decay in the rotational diffusion limit (eq 9), one may write

$$\tau_{rot} = \xi I/6kT = f\eta V/kT \qquad (11)$$

The influence of the shape of the molecule is contained in the geometrical shape factor f, which can be seen in the stick limit to be equal to ${}^2/_3$ times the β-dependent term in eq 10. When the body is spherical ($\beta = 1$), one finds from eq 10 that $\lim_{\beta\to 1}\xi_{stick} = 6\eta V/I$, corresponding to $f_{stick} = 1$. The value of τ_{rot} in the slip limit follows from the use of eq 11 with $f_{slip} = f_{stick}\xi_{slip}/\xi_{stick}$.

(A) *J*- and *m*-Diffusion Models.[6] To overcome the restriction to small angular steps for the free rotation between collisions, which clearly limits the preceding theories to relatively high densities, Gordon developed the *J*- and *m*-diffusion models.[6] In these purely collisional models, the interaction of solute and solvent results solely from discrete, Poisson-distributed events ("collisions") with collision interval τ_{coll}. Between collisions, free rotation of the rotor pertains, and arbitrarily large angular excursions under free inertial motion are possible at large τ_{coll}.

In the Gordon models, the key to obtaining a closed form solution for the polarization anisotropy is the assumption that the direction of $\vec{j}$ is randomized at each collision. In the *m*-diffusion model, the magnitude j remains constant, while in the more realistic *J*-diffusion model the magnitude is also randomized over a thermal distribution at each collision. The assumption of angular momentum randomization at each collision means that the angular velocities before and after a collision are uncorrelated ($\langle\vec{\omega}(\tau_{coll}^-)\cdot\vec{\omega}(\tau_{coll}^+)\rangle = 0$). Thus, the only contribution to the angular velocity autocorrelation function

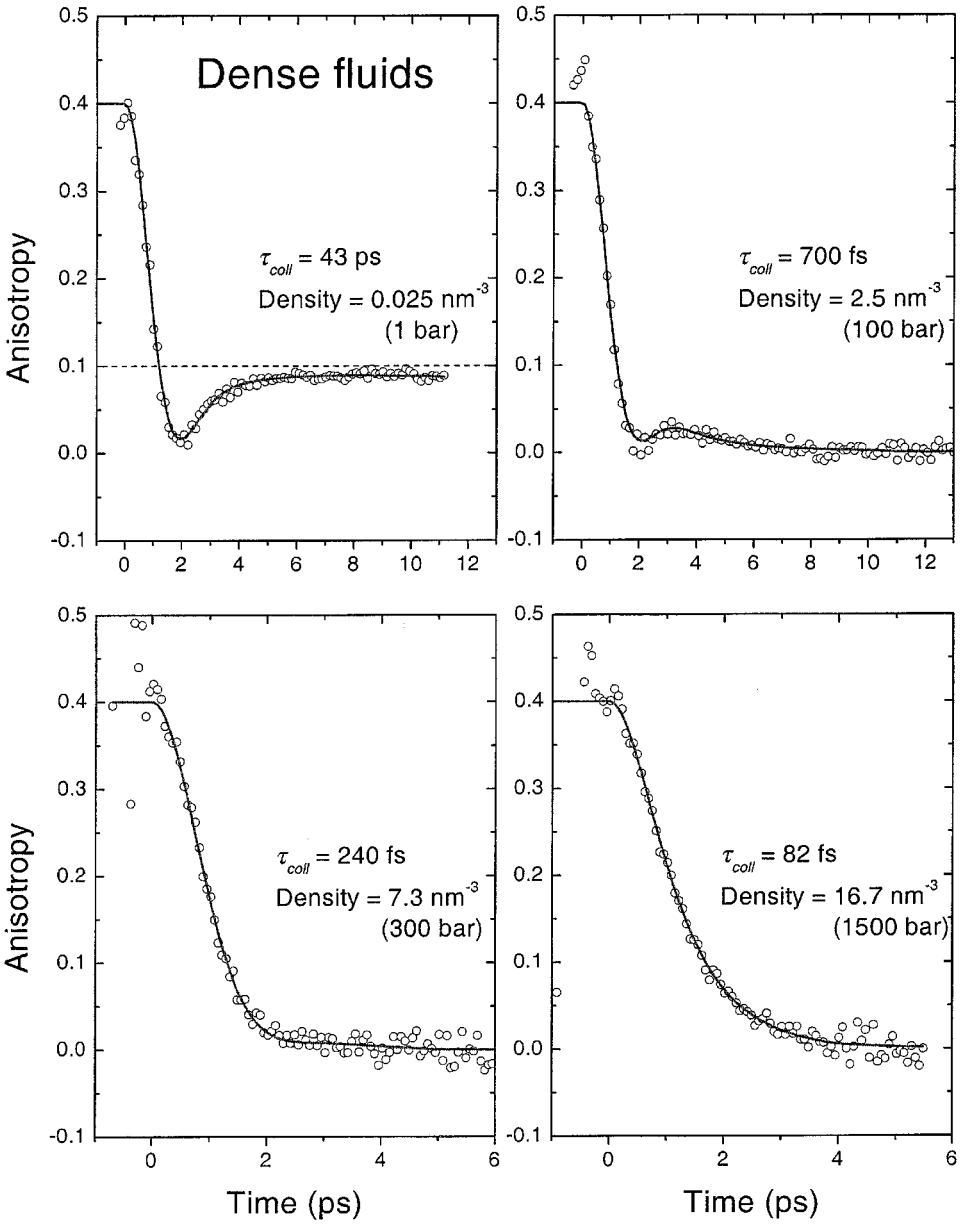

Figure 5. *J*-coherence fits of experimental polarization anisotropies of iodine in argon at a range of densities. The *J*-coherence collision time, and the number density and pressure of the solvent are shown for each anisotropy. λ_{pump} is 613 nm for the 300 bar data, and 623 nm for the other three.

comes from the population which has suffered no collisions. According to the Poisson distribution, this population decays exponentially with time constant τ_{coll}; that is, $\tau = \tau_{coll}$.

The assumptions underlying each of the above treatments preclude the quantitative prediction of dynamic behavior as a function of the physical nature of the solvent particles. The gradual transition of the polarization anisotropy from its distinctive and nonmonotonic free-rotor form to a diffusion-controlled exponential decay at long time and nonzero pressure is approximated in the Gordon models, although not quantitatively and without explicit solvent dependence, while Langevin-hydrodynamic treatments are invalid under conditions of large-angle free (inertial) rotation and therefore cannot reproduce the coherence associated therewith. In contrast, the quantitative features of the measured rotational dynamics are captured for a broad range of densities by the *J*-coherence model, which is summarized below.

(B) *J*-Coherence Model.[13] To establish the link between the physical parameters of the solute−solvent system in question, including the masses, moment of inertia, temperature, and the intermolecular potential, and the friction, or decay of $\Omega(t)$, the Gordon assumption of randomization of $\vec{j}$ is replaced by an approximation of the specific distribution of final $\vec{j}$, which is produced by the kinematics of the actual binary collisions. The general framework of the Gordon models is retained, but following the *n*th collision, the distribution of $\vec{j}_{n+1}$ is not thermal, but given by the function $P_{\vec{j}}(\vec{j}_n,T,m)$, which incorporates a precise classical hard-sphere treatment of the collision of the rotor with a solvent atom of mass *m*, at solvent temperature *T*. The anisotropy decay of the sample is obtained by numerically tracking the rotational trajectories of a large number of molecules through binary collisions with a statistical selection of solvent atoms. In this way, the relationship between the true collision interval, as derived from kinetic gas treatments, and τ, the effective angular momentum scrambling lifetime, is determined.

In Figure 5, measured anisotropy decays of iodine in argon are shown with *J*-coherence model fits.[13] One sees that the general features of the experimental anisotropies across the full range of densities are well-reproduced by the theory. The free-

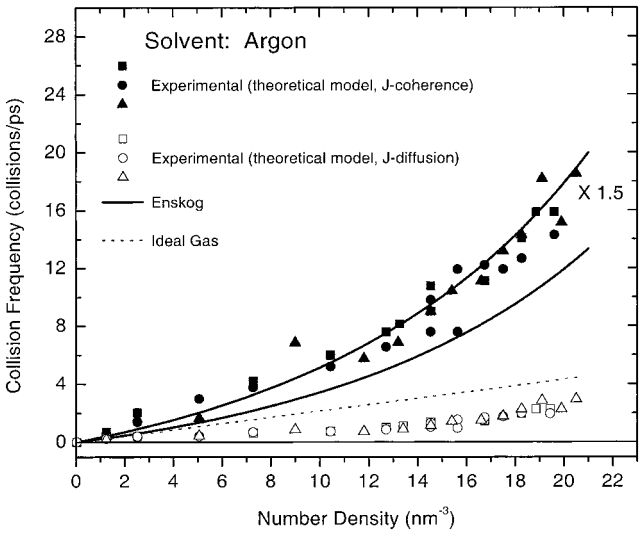

Figure 6. Solvent density dependence of the collision rates of iodine in argon derived from experimental anisotropies by the *J*-coherence and *J*-diffusion models. Different symbols correspond to independent series of experiments. The hard-sphere ideal-gas and Enskog collision rates are shown for comparison. The Enskog curve is plotted a second time scaled by a factor of 1.5.

rotor anisotropy, characterized by a coherent dip (at which the average rotor is approximately perpendicular to its initial direction) followed by a gradual return to the asymptotic value of 0.1, is approximated by the 1 bar argon measurement in Figure 5.

At higher pressures, the dip is washed out when collisions scramble the angular momentum alignment before the initial *dipole* alignment is totally lost (first $^1/_4$ period of rotation). At very high pressures, the dipoles undergo a relatively slow monotonic angular diffusion toward isotropy, reflected by an exponentially decaying $r(t)$. The data in ref 13 illustrate very clearly, however, that the transition from low to high pressure limits has a very different density dependence in the solvent gases argon and helium. For example, the anisotropy dip has completely vanished by a density of 7.3 argon atoms/nm^3 (300 bar). Above this pressure of argon, it is possible to obtain a good fit of the anisotropy using the Langevin friction model and eq 7. In contrast, the anisotropy dip in helium is still very evident at 20 atoms/nm^3 (1300 bar), and the anisotropy does not fit well to the Langevin friction model even at 26.6 helium atoms/nm^3, indicating partial coherence of rotational motion survives for delays up to at least 4 ps.

From the *J*-coherence calculations, both the anisotropy and $\Omega(t)$ were obtained. $\Omega(t)$ was single exponential in form and its lifetime τ could be compared with τ_{coll} to quantify the j scrambling potency per collision of each solvent. It was found that, $\tau = 5.5\tau_{coll}$ for argon and $\tau = 43\tau_{coll}$ for helium. That is, the angular velocity of an average iodine molecule persists through ~5.5 collisions with argon and 43 collisions with helium.

In addition to accurately reproducing the temporal evolution of the anisotropy at arbitrary density, a primary goal of the *J*-coherence model is to be able to predict its dependence on the properties of the solvent. In Figure 6, the Enskog hard-sphere collision rate vs density is shown as derived independently of the experiments. The experimental *J*-coherence collision rates in argon are only slightly higher than the Enskog rates, showing good agreement with a scaling of the rates by a factor of 1.5. For helium, in which collisions with iodine are well-represented by a hard sphere potential, the rates are in very good agreement with the Enskog rates without adjustment.[13]

In summary, the *J*-coherence bimolecular collision model provides a clear prescription for relating the hard-sphere properties of the solvent and solute to the friction and to the decay of solute anisotropy over the entire experimental density range, from free rotational motion to rotational diffusion. In a recent article,[25] Gelin has related the *J*-coherence model to the Keilson-Storer model and presented analytical expressions yielding results that are in close agreement with those of the *J*-coherence analysis.

IV. Orientation in Liquids and Solutions of Confined Molecules

As seen in the case represented in Figure 5, when the angular momentum correlation time becomes shorter than the characteristic time scale of free rotation, a diffusive description of rotational motion is appropriate. This limit generally applies for molecules in solution, but the form of the anisotropy decay need not be the simple one of eq 9. For an asymmetric solute molecule with arbitrary transition moment directions, the general form of $r(t)$ has up to five exponential components with lifetimes that are functions of the diffusion constants for rotation about the three principal axes.[4] The required generalization of eq 10 for the sticking friction coefficients for rotation of an arbitrary ellipsoid about each of its principal axes can be found in ref 3, and the corresponding slip coefficients are available for a range of ellipsoid shapes.[26]

With these theoretical results in hand, the effective local friction coefficients for a wide variety of solute−solvent systems have been deduced from measured anisotropy decays. Comparison with the limiting hydrodynamic values suggests significant variability in the effective boundary condition, ranging from slip to stick and sometimes beyond. Extensive discussion of these results and the models advanced to provide a microscopic explanation for the variability in boundary condition can be found elsewhere.[27]

In liquids and solutions, the observation of the decay of $r(t)$ in real time provides a direct view of the nature of local friction and the degree of orientational freedom of the solute. The former is evident in the time scale of the decay of $r(t)$, while a barrier to free motion may be reflected by decay of the anisotropy to a nonzero value, ranging from zero for unrestricted motion to 0.4 for a system in which rotation is completely hindered. A striking example is given in Figure 7 for a dye molecule (HPMO) in solution, in a micelle, in cyclodextrin, and in a protein.[28] In *p*-dioxane solution, the anisotropy decays by simple isotropic diffusion. In the protein, a constant value of the anisotropy shows that the dye is effectively immobilized on the time scale of the experiment, while in cyclodextrin, in particular, partial orientational relaxation to a long-lived plateau of $r(t)$ is clear evidence of restricted motion of the dye within the sugar cavity. Similar studies have been made in this laboratory to examine the nature of confined hydrophobic structures in proteins and their recognition of DNA.

V. Orientation in Reactions

The concept of collision-induced angular momentum scrambling of section III is relevant also to the dynamics of reactive systems, where now the recoil from fragmentation parallels the effect of impact with a solvent molecule. Thus, polarization anisotropy measurements are likewise of value in providing a view of the temporal change in vectorial dynamics in time-resolved studies of dissociation reactions.[29,30] In a previous

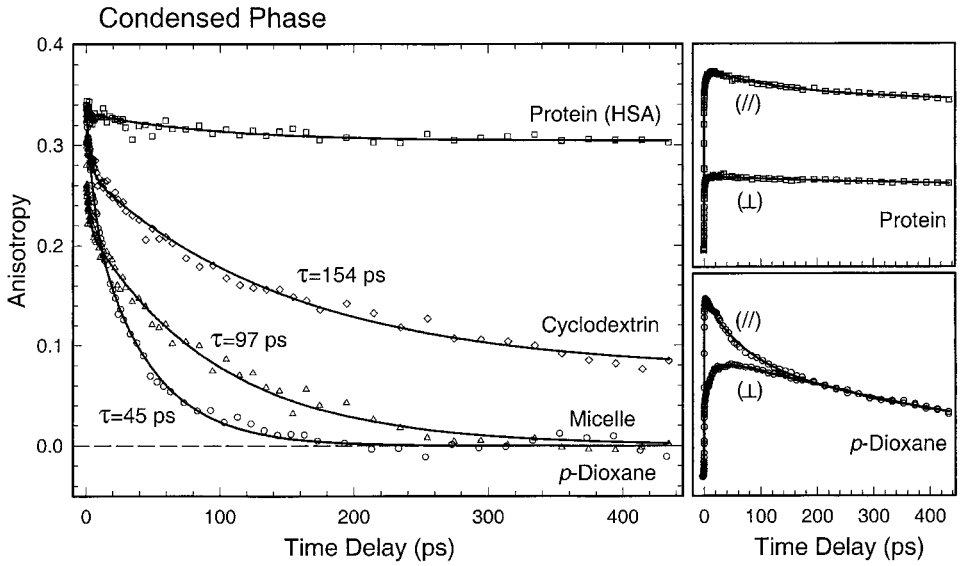

Figure 7. Femtosecond-resolved fluorescence anisotropy evolution of the dye molecule HPMO in four typical environments at 470 nm emission. The corresponding polarization-analyzed transients for two of the environments are shown at the right.

study,[8] we presented a classical treatment of time-dependent coherent alignment in the products of a unimolecular dissociation initiated by pulsed laser excitation, based on the simplifying assumptions of prompt, impulsive dissociation and symmetric top motion. Despite the high degree of approximation underlying the calculations, certain features of experimental measurements were qualitatively reproduced, providing potentially valuable insight into the dissociation vectorial dynamics.

(A) Evolution of Coherence. Consider systems that dissociate into atom + molecule, i.e.,

$$M_1 \rightarrow M_1^* \rightarrow M_2 + A \qquad (12)$$

with M_2 ranging from a diatomic to a large polyatomic. Such a reaction is illustrated at the bottom of Figure 8. Here, the polarized pump pulse creates a spatial alignment of the *reactant* (M_1^*) population from an initially isotropic M_1 population, and the time evolution of alignment of the dipole moment, $\hat{\mu}_2$, of the *product* molecules determines the time-dependent polarization anisotropy of the signal. The translational motion of the fragments in the M_1^* center of mass frame is characterized by separation of the centers of mass of M_2 and A with equal and opposite linear momenta, along trajectories that are displaced from each other by the impact parameter *b*. The energy difference E' between the internal energy of M_1^* and that of the products appears as kinetic energy of rotation and translation.

To calculate the time dependence of the probe signal as a function of probe polarization for the reaction described by eq 12, the rotational motion of each probe dipole must be traced continuously from $t = 0$, the moment when the alignment of the reactant population M_1^* is created by the excitation pulse. In a "prompt, impulsive dissociation" approximation, the motion of M_1^* prior to dissociation and the duration of the "transition state" between reactant and free product are both taken to be of negligible duration when compared with the rotational periods entering significantly into the calculation. In this case, only the initial molecular structure, the direction of the impulse in the molecular frame, and the available energy E' need be specified. Although it is assumed here that the fragment M_2 evolves as a free molecule from $t = 0$, this problem differs in general from that posed by the direct excitation of M_2 in an isotropic sample, since dissociation may lead to a quite different rotational state distribution.

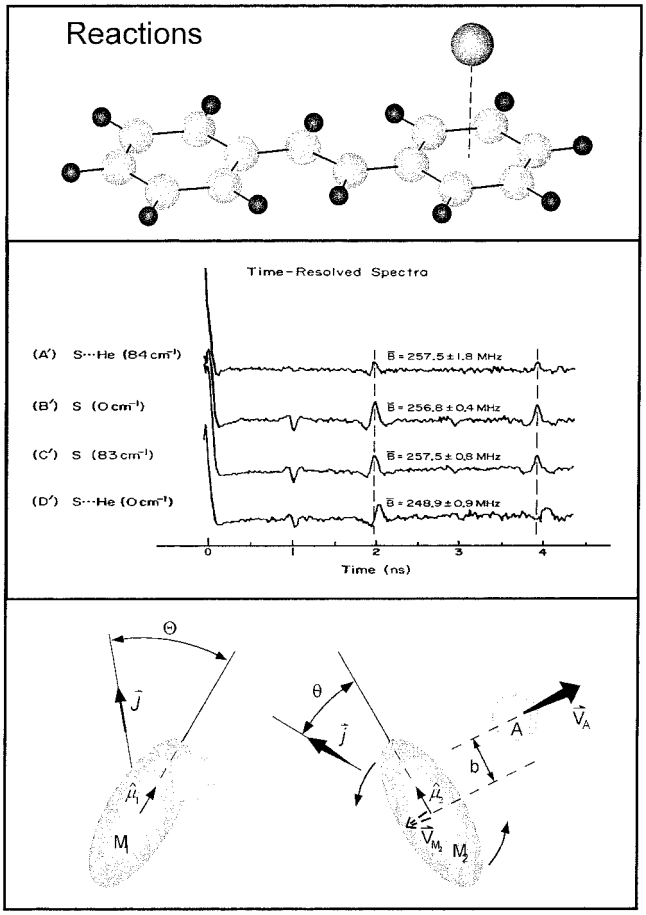

Figure 8. Orientation in reactions. (Top) Approximate molecular structure of the *trans*-stilbene−He_1 van der Waals complex. (Middle) Time-resolved anisotropies pumping two different absorption bands of *trans*-stilbene (S) and the *trans*-stilbene−He_1 complex (S···He). Excitation energies relative to the respective (complex or parent molecule) electronic origins are given. $\bar{B}$ is $^1/_2(B' + C')$ of the complex or parent stilbene (see ref 29). (Bottom) Geometry of the dissociation problem, $M_1 \rightarrow M_1^* \rightarrow M_2 + A$. Left: Before excitation by the pump pulse of transition dipole $\hat{\mu}_1$ of M_1. Right: After dissociation, the dipole $\hat{\mu}_2$ of fragment M_2 is probed.

As initial conditions for the dissociation experiment, i.e., prior to the pump laser pulse, we assume that a rotational state

population distribution $P_J(\{i\})$ of M_1 molecules in a single vibronic state is accessible to the pump laser, where $\{i\}$ represents any complete set of rotational coordinates for M_1, and that the population is spatially isotropic. The orientational evolution that is pertinent to the pump/probe process is completely expressed in the function $\hat{\mu}_1(\{i\},0)\cdot\hat{\mu}_2(\{f\},t)$, as in eq 2, but where now, due to the dissociation process, the initial and final rotational states generally differ. In the prompt, impulsive approximation, $\hat{\mu}_1(\{i\},0)\cdot\hat{\mu}_2(\{f\},t)$ does not depend on $\{i\}$, so the state-resolved anisotropy does not either. Only the ensemble average of eq 2 may depend on $\{i\}$ through the influence it exerts on $P_j(j,\theta,\psi_0)$, the distribution of final rotational state populations.

As an example, consider a case in which both pump and probe dipoles are parallel to the symmetry axis of M_2, as illustrated at the bottom of Figure 8. The $\{f\}$-state-resolved $r(j,\theta,\psi_0,t)$ is clearly equivalent to the (||,||) dipole case given by eq 3, and thus again does not depend on ψ_0, which specifies the azimuthal orientation of $\vec{j}$ in the M_2-fixed frame. Because the same anisotropy is displayed by all fragments occupying a common energy level, the *energy-level*-resolved anisotropy of the (||,||) dipole case following prompt, impulsive dissociation is also identical to that for direct excitation of free stable molecules, despite the fact that in the latter ψ_0 is uniformly distributed over 2π, while the distribution of ψ_0 following dissociation will normally be very nonuniform. Note that the macroscopic anisotropies in the two cases will in general still be different, however, reflecting different final energy level population distributions.

In the general case, the function $P_j(j,\theta,\psi_0) \equiv P_j(\vec{j})$ can be related directly to the three physical sources of M_2 rotation: (i) initial rotation of M_1, (ii) the torque applied by repulsion between M_2 and A as they dissociate, and (iii) initial vibration of M_1. When a rigidly rotating molecule dissociates impulsively, the final angular momentum of M_2 is composed of two independent contributions from sources (i) and (ii). The contribution of the torque, $\vec{j}_t$, can be calculated by invoking conservation of energy and momentum:[8]

$$\vec{j}_t = \left(\frac{2E'}{1/\mu b^2 + (\mathbf{II}^{-1}\hat{t})\cdot\hat{t}}\right)^{1/2}\hat{t} \qquad (13)$$

where **II** is the inertia tensor of M_2, $\hat{t}$ is a unit vector in the direction of the torque applied to M_2, and μ is the reduced mass of A and M_2.

When the initial angular momentum distribution is thermal ($P_J(\vec{J}) = N/(\pi Q)\exp(-E(\vec{J})/kT)$) the final angular momentum distribution, accounting for both initial rotation and torque, can be expressed as

$$P_j(\vec{j}) \propto \exp[-(\mathbf{FG}(\vec{j} - \vec{j}_t))^2] \qquad (14)$$

for matrices **F** and **G** defined in ref 8 as functions of the structural parameters of M_1 and initial rotational temperature. The effect of initial vibration of M_1 on $\vec{j}$, and on $\vec{j}_t$ in particular, can be major, however, so the distribution of geometries associated with vibrational motion may not be neglected in general. A simple model of the role of vibration can be realized by averaging the rigid body dissociation described by eq 14 over a distribution of positions of A along the appropriate coordinate.

Equations 14, 13, and A-5, combined with the state-resolved anisotropy (eqs A-1, A-2, and $r_{\hat{\mu}_1\hat{\mu}_2}(j,\theta,\psi_0,t) = 0.4P_2[\hat{\mu}_1(0)\cdot\hat{\mu}_2(t)]$) constitute a general framework for calculation of the observable, macroscopic anisotropies of dissociation products. Such calculations may be compared with specific experimental results to infer a product rotational distribution and interpret the distribution in terms of the dynamics of dissociation.

(B) Theory vs Experiment. The vibrational predissociation of the *trans*-stilbene−He_1 van der Waals complex offers one chance for such a comparison of theory and experiment. The S_1 dissociation dynamics of *trans*-stilbene−X (X = He, Ar, Ne) complexes at low excess vibrational energies have been studied in our laboratory by picosecond time-resolved fluorescence detection.[31,32] To investigate the effect of dissociation on the dynamics of product rotation, stilbene product emission was polarization-analyzed. The result for 84 cm^{-1} excitation is shown in Figure 8 in the form of the experimental polarization anisotropy $R(t)$. Shown also in the figure, for comparison, are anisotropies of parent stilbene for two excitation energies and of S−He excited to its S_1 origin.

In addition to the initial decay and dip of the anisotropy, the data of Figure 8 display prominent recurrences, though they are distinctly weaker in the anisotropy of the dissociation product than in the three other cases. The reduction in amplitude appears particularly severe for the negative or out-of-phase recurrences. The recurrence period is seen to match the nutation period of stilbene rather than that of the initially excited complex, thereby confirming that the emitter is stilbene.

To compare with theory, calculations were performed for product stilbene undergoing symmetric top motion following dissociation. (It can be confirmed that rotation is sufficiently slow compared to the dissociation lifetime (~40 ps) and the duration of interaction after dissociation (~1 ps) that the prompt and, particularly, the impulsive assumptions are reasonable in this case.[8]) The calculation of prompt, impulsive dissociation from the equilibrium geometry (shown at the top of Figure 8, helium coordinates relative to the *trans*-stilbene center of mass of $x_A \sim 0$, $y_A = 3.0$ Å, and $z_A = 3.15$ Å, with the long axis of stilbene labeled *z* and *xz* being the stilbene plane) results in a reduction of about 30% of the in-phase recurrence, while that observed in the first in-phase recurrence of the experimental data was typically about 40%.

In the simulation, the effect results from the fact that each stilbene product molecule retains almost all of the initial angular momentum of the complex ($\vec{J} \sim 10\hbar$), and the impulse adds to that an angular momentum of $|\vec{j}_t| \sim 10\hbar$. Although the addition is vectorial and therefore reduces the total angular momentum of some molecules while increasing that of others, the increases dominate and the effective rotational temperature of the sample is raised. Higher temperature has the effect, in conjunction with convolution with the instrument response, of reducing measured recurrence amplitudes.[15]

Although the experimental reduction of the in-phase recurrence is similar to that predicted by the model calculation, the out-of-phase recurrences seem to be more severely damped in the measured anisotropies. A simple extension of the model to include a distribution of initial geometries was made to investigate the role of vibrational averaging and see if this might account for the above difference. A long axis displacement of the helium (i.e., an average over a distribution of z_A) has no great effect on the calculated anisotropy. A stretch of the van der Waals bond has no effect at all since the impulsive force is normal to the stilbene plane. However, calculation of the anisotropy for a perpendicular bend distribution shows that contributions from off-axis geometries do produce noticeably smaller out-of-phase recurrences.

Another reaction for which theory and experiment have been compared is the dissociation of room-temperature ICN following

308 nm excitation.[8] Femtosecond measurements with polarized pump and probe pulses revealed an initial anisotropy of the signal that decayed on a subpicosecond time scale. In this case, very little parent rotation carries over to the CN ground-state product, so the hot CN rotational distribution is a consequence of a large impulsive torque acting in a nonlinear configuration. A significant aspect of this study was the fact that the laser bandwidths limited contributions to the average in eq 2 to only a small subset of all populated states for any one experiment.

A third example of time-dependent alignment in reactions is the femtosecond dissociation of HgI_2 at 308 nm[8] via two reaction channels, one producing ground-state iodine ($^2P_{3/2}$) and the other spin−orbit excited I* ($^2P_{1/2}$), with product HgI being vibrationally coherent. The measured anisotropy could be simulated only with very significant $\vec{j}_t$ contributions (eq 13), which required not only that dissociation occur predominantly in bent configurations, but also that higher bend angles lead preferentially to the production of ground-state iodine. Studies of the polarization-analyzed signals of this reaction proved essential in showing the vectorial, orientational motion of liberated HgI, and scalar vibrational (coherent) dynamics of HgI as it separates from the force field of the I atom. Femtosecond anisotropy measurements have also been carried out in solution for this reaction, and vibrational coherence also persists in solution.[33,34]

These examples suggest the manner in which information about vectorial reaction dynamics may be obtained from polarization anisotropy measurements. Such measurements reflect the rotational distribution of the fragment, from which may be deduced information about: (i) the nature of the applied torque, and (ii) the geometry of the initial complex. These two aspects of the reaction are closely related to each other, and can be extracted from the measurements by taking into account the available energy and contribution of parent rotation to the fragment. The method should be particularly appropriate for use on large fragments for which the *shape* of rotational recurrences reflect the asymptotic rotational distribution, in the same way that their *separation* identifies the fragment molecular structure.

VI. Orientation in Space and Time: the Classical Limit

We give here a specific, concrete illustration of orientational anisotropy from the quantum mechanical perspective, with emphasis on the importance of time scale in reaching classical-like behavior. We consider a linear molecule whose orientational properties are completely described by rotational wave functions $\Psi_{jm}(\theta,\varphi)$, where θ and φ are polar coordinates for the orientation of the nuclear axis in the lab frame and m is the quantum number for the projection of the angular momentum on the laboratory Z axis.

We have, for j any positive integer and integral m ranging from j to $-j$,[35]

$$\Psi_{jm}(\theta,\varphi) = \sqrt{\frac{(2j+1)(j-|m|)!}{4\pi(j+|m|)!}} P_j^{|m|}(\cos\theta) e^{imp} \quad (15)$$

where $P_j^{|m|}(\cos\theta)$ is an associated Legendre function, that may be explicitly expressed as

$$P_j^{|m|}(\cos\theta) = \sin^{|m|}\theta \sum_{n=0}^{\nu} (-1)^n \times \frac{(2j-2n)!}{2^j n!(j-n)!(j-2n-|m|)!} \cos^{j-2n-|m|}\theta \quad (16)$$

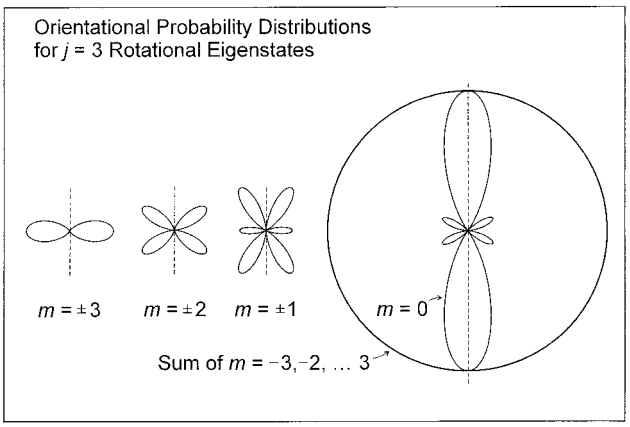

Figure 9. Orientational probability distributions for $j = 3$ rotational eigenstates, and for the ensemble average of the seven m sublevels. In this and Figures 10 and 11, the distributions all have axial symmetry about the z-axis (dashed line).

with $\nu = (j - |m|)/2$ if $(j - |m|)$ is even, or $(j - |m| - 1)/2$ otherwise. The orientational probability density of a molecule in the (j,m) rotational eigenstate is given by $|\Psi_{jm}(\theta,\varphi)|^2$. Examples of the orientational densities for $j = 3$ are shown in Figure 9. Note that, despite the complicated distributions for individual m values, the spatial distribution of the sum of the seven equally populated (in a thermal, field-free sample) m sublevels is isotropic, exactly as in the classical case. The same is true for the sum of the $2j + 1$ m sublevels for any j, as shown by application of the spherical harmonic addition theory.

The transition probability for electronic excitation of a molecule depends on the transition dipole direction in the molecular frame, the laser polarization, and the initial and final rotational states.[36] As a specific example, we assume a transition dipole vector parallel to the nuclear axis and laser polarization parallel to the laboratory Z axis. In this case, only transitions $j' = j'' - 1$, $m' = m''$ (P branch) and $j' = j'' + 1$, $m' = m''$ (R branch) are possible, with amplitude factors proportional to $\sqrt{(j''-m''^2)/(4j''^2-1)}$ and $\sqrt{((j''+1)^2-m''^2)/((2j''+1)(2j''+3))}$, respectively.

An appropriately tuned narrow bandwidth laser will access a branch-specific transition of all m'' sublevels of a given j'', thereby creating an excited-state ensemble with the relative contribution of each excited state m' sublevel weighted by the square of the appropriate factor given above. These weights clearly favor excitation of low $|m|$, which, given the m dependence of the densities exemplified in Figure 9, means that the orientational distribution of the excited state ensemble will be skewed toward the Z axis. This is at least qualitatively consistent with expectations, given that the transition dipole is coincident with the nuclear axis. The branch-resolved orientational distributions for $j'' = 3$ are shown in Figure 10; with the mentioned selection rules, only $j' = 2$ or $j' = 4$, with $\Delta m = 0$ are reached. Because each molecule occupies a single rotational eigenstate in the excited state, all distributions are *time-independent*. The total P branch (top right) and R branch (bottom right) distributions are each less strongly oriented than cosine-squared, while the individual m states have very complex structures, as shown in the figure.

On the other hand, a sufficiently short pulsed excitation may coherently excite both P and R transitions in each molecule, creating an excited superposition state (rotational wave packet,

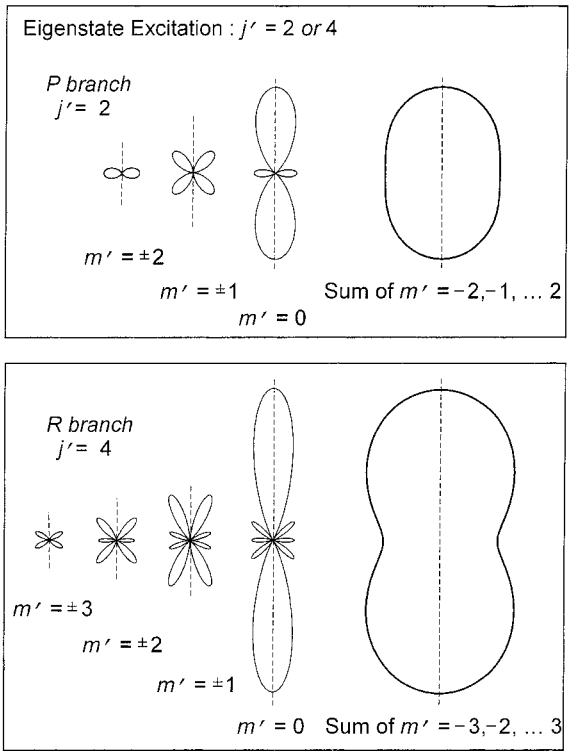

Figure 10. Branch-resolved excited-state orientational probability distributions for cw excitation of the m sublevels of $j'' = 3$, and the corresponding total distributions.

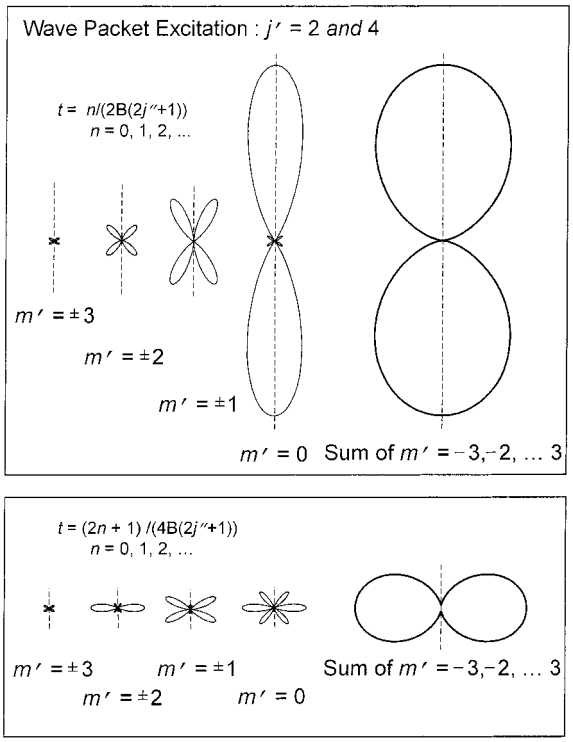

Figure 11. Excited-state orientational probability distributions for femtosecond excitation of the m sublevels of $j'' = 3$, and for the total ensemble, shown at two times. (Top) The initial distribution, which recurs periodically ($t = n/(2B'(2j'' + 1))$, $n = 0, 1, 2, ...$). (Bottom) Distribution at odd multiples of half the recurrence period ($t = (2n + 1)/(4B'(2j'' + 1))$, $n = 0, 1, 2, ...$).

$\Psi_{\mathrm{rot}}^{\mathrm{wp}}(t)$) of the form

$$\sqrt{\frac{j^2 - m^2}{4j^2 - 1}}\Psi_{j-1m}(\theta,\varphi)\mathrm{e}^{-i(hB'(j-1)j)t/\hbar} + \sqrt{\frac{(j+1)^2 - m^2}{(2j+1)(2j+3)}}\Psi_{j+1m}(\theta,\varphi)\mathrm{e}^{-i(hB'(j+1)(j+2))t/\hbar}$$

where $''$ has been omitted from all j's and m's. The unequal temporal phase factors in the two terms of this superposition state lead to a time-dependent cross-term in the excited-state probability distribution, $|\Psi_{\mathrm{rot}}^{\mathrm{wp}}(t)|^2$, that is modulated at the frequency $2B'(2j'' + 1)$ (i.e., $\omega = (2j'' + 1)\omega_{\mathrm{no}}$). The excited-state distributions for each m'' ($=m'$), and their sum, are shown at two different times in Figure 11, again for $j'' = 3$. The initial total distribution (top right) is *exactly* equal to the classical cosine-squared, and it recurs periodically as indicated. At odd-multiples of half the recurrence period, the ensemble distribution (bottom right) approaches the classical $^1/_2 \sin^2 \theta$, even at $j'' = 3$, and equals it exactly in the limit of high j.

Note, however, that, when the excited state is short-lived, the absorption strength of rotational eigenstates is spectrally broadened, allowing rotational wave packets to be created *even with a cw laser*. Since these wave packets evolve as in the femtosecond excitation experiments, high levels of anisotropy can be measured, reflecting the classical orientation averaged over an excited state lifetime shorter than its rotation time. On the basis of this fact, steady-state anisotropy values and product angular distributions are commonly used to deduce how excited-state lifetimes (or fragmentation lifetimes) compare with rotation times.

VII. Some Remarks Regarding Applicability

We have attempted to convey in the preceding sections an understanding for the fundamental relationship between orientational dynamics, molecular structures, and time-resolved anisotropy measurements in a wide range of environments. In interpreting all such measurements, it is necessary to be aware of the requirements for the applicability of the theoretical treatments outlined here. The general expressions, eqs 1 and 2, are valid for detection schemes that produce a signal proportional to the one-photon absorption probabilities for both the pump and probe process. If either of the transitions is in a regime of saturation (nonlinear power dependence), this condition is clearly not met and the anisotropic response to the polarized light will be reduced.

Likewise, a detection scheme whereby the probe transition transfers population to an otherwise unoccupied vibronic level, and that population is monitored subsequently (in what can be called pump/probe/detect schemes), consideration must be given to possible influence on the monitored attribute of the high degree of alignment created in the pump/probe steps. When the detection process is either fluorescence detection or absorption of a third light pulse, the proper choice of detection polarization for pump and probe parallel or perpendicular to each other is one that forms equal angles with an orthogonal axis system defined by the pump and probe polarization directions. Any other choice of detection polarization can modify the form of the anisotropy.[8,37]

In the case of measurements by pump−probe ionization mass spectrometry, caution is also warranted in applying the standard theories described here, which assume transition dipoles that have rigorously defined directions in the molecular frame, as in the case of neutral−neutral transitions The additional degrees of freedom of the ionization step (to ion + free electron) demands care in the treatment of the angular dependence of alignment.[38]

Another underlying assumption of the treatments outlined here is that the structures probed reorient under their respective influences as rigid molecules with fixed transition dipoles. It is clear that any process of internal structural or electronic relaxation that results in internal reorientation of the transition dipole may be detectable as a change in the anisotropy that is unrelated to rotation of the molecule as a whole. Since electronic excitation often leads to rapid relaxation or reorganization, such anisotropy effects are relatively common and provide one avenue to investigate the internal state of the excited molecule.

A final note on applicability concerns the experimental detection of fluorescence by the up-conversion method, where the sample fluorescence is time-gated by sum-frequency mixing with an ultrashort gating light pulse in a nonlinear crystal. This technique is equivalent in principle to polarized fluorescence detection by time-correlated single-photon counting (TCSPC), but with time resolution dependent only on the gating pulse width. However, the difference in sensitivity between direct fluorescence detection by photomultiplier and the up-conversion method has the practical consequence that fluorescence in up-conversion is typically collected over large solid angles by means of parabolic mirrors. Such collection reduces polarization selectivity. In this case, for example, even when excitation and emission involve only two electronic states and hence occur via the same transition dipole, the measured initial anisotropy value may be systematically smaller than the theoretical value of 0.4. The same problem will be encountered in TCSPC if the solid angle for fluorescence collection is made large.

VIII. Conclusion

It has been our hope in this contribution to summarize, and provide substantial insight into, some of the basic concepts that have been important to the efforts of the Caltech research group in the area of time-resolved molecular anisotropy. Study of orientation in real time is powerful in elucidating the vectorial dynamics in reactive and nonreactive systems and in obtaining direct information on molecular structures. For achieving real classical orientation of molecules (governed by $\vec{\mu}\cdot\vec{\epsilon}$) by creation of classical-like wave packets, the femtosecond time resolution is ideal, allowing for the study of orientation change in real time and in the different phases discussed here: gases/molecular beams, dense fluids, liquids, and solutions of confined molecules. On this time scale, coherent superposition of eigenstates allows for the nonstationary-state evolution of orientation because the time duration of the pulse (or generally the coherence time of the source) is much shorter than the rotational period for orientation; a superposition may also appear under cw excitation, but only for a short-lived excited state and/or when the dephasing time is sufficiently short. The vectorial dynamics are manifestations of stereochemical properties and their studies give a direct view of dynamical phenomena such as coherent inertial motion and recurrences, collision dynamics, microscopic friction/viscosity, and local rigidity.

IX. Appendix

In this appendix we collect those equations necessary for the calculation of $r(t)$ for a classical symmetric top molecule, restricted only by the requirement that pump and probe dipoles lie in a common plane containing the molecular figure axis.

To derive the form which the key function $\hat{\mu}_1(0)\cdot\hat{\mu}_2(t)$ takes, we refer to Figure 12, in which θ, φ, and ψ are Euler angles relating a molecule's principal inertial axes (x, y, z) to space fixed axes (X, Y, Z), chosen for each molecule so that the Z axis lies along $\vec{j}$. When z is the unique axis of the symmetric top, the rotational motion of the top manifests itself as changes in the angles φ and ψ at the constant angular velocities ω_n and ω_r, respectively. Thus, the time-dependent molecule-fixed axes obey the following equations:

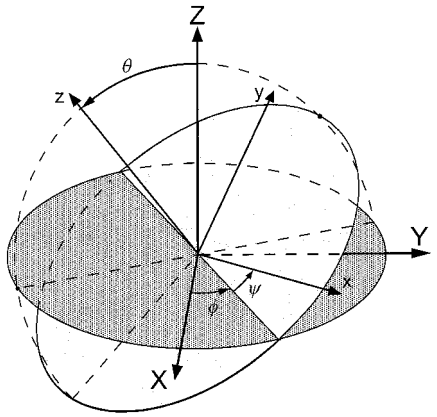

Figure 12. Euler angles specifying the orientation of the molecule-fixed reference frame (x, y, z) relative to the lab-fixed frame (X, Y, Z). For the derivation of eq A-1, Z is chosen to coincide with the angular momentum of the molecule, and z with the molecular figure axis.

$$\hat{x}(t) = (\cos(\psi_0 + \omega_r t)\cos\omega_n t - \cos\theta \sin(\psi_0 + \omega_r t)\sin\omega_n t)\hat{X} + (\cos\theta \sin(\psi_0 + \omega_r t)\cos\omega_n t + \cos(\psi_0 + \omega_r t)\sin\omega_n t)\hat{Y} + \sin\theta \sin(\psi_0 + \omega_r t)\hat{Z} \quad \text{(A-1a)}$$

$$\hat{y}(t) = (-\sin(\psi_0 + \omega_r t)\cos\omega_n t - \cos\theta \cos(\psi_0 + \omega_r t)\sin\omega_n t)\hat{X} + (\cos\theta \cos(\psi_0 + \omega_r t)\cos\omega_n t - \sin(\psi_0 + \omega_r t)\sin\omega_n t)\hat{Y} + \sin\theta \cos(\psi_0 + \omega_r t)\hat{Z} \quad \text{(A-1b)}$$

$$\hat{z}(t) = (\sin\theta \sin\omega_n t)\hat{X} - (\sin\theta \cos\omega_n t)\hat{Y} + \cos\theta\hat{Z} \quad \text{(A-1c)}$$

where the arbitrary value of φ_0 has been taken as 0, and the angular frequencies are $\omega_n = \omega_{no}j$ and $\omega_r = \omega_{ro}k$ (see text).

Since the quantity $\hat{\mu}_1(0)\cdot\hat{\mu}_2(t)$ can be expressed as

$$\hat{\mu}_1(0)\cdot\hat{\mu}_2(t) = (\mu_{1x}\hat{x}(0) + \mu_{1y}\hat{y}(0) + \mu_{1z}\hat{z}(0))\cdot(\mu_{2x}\hat{x}(t) + \mu_{2y}\hat{y}(t) + \mu_{2z}\hat{z}(t)) \quad \text{(A-2)}$$

where μ_{ia} is the projection of $\hat{\mu}_i$ on the molecule-fixed a-axis, eqs A-1 and A-2 and the relation $r_{\hat{\mu}_1\hat{\mu}_2}(j,\theta,\psi_0,t) = 0.4P_2[\hat{\mu}_1(0)\cdot\hat{\mu}_2(t)]$ provide a complete prescription for calculation of the state-resolved probe signal anisotropies, $r_{\hat{\mu}_1\hat{\mu}_2}(j,\theta,\psi_0,t)$.

In general, $\hat{\mu}_1(0)\cdot\hat{\mu}_2(t)$ depends on ψ_0, the initial rotational phase angle, which has no influence on rotational energy. In a statistical ensemble of free molecules, ψ_0 will therefore be uniformly distributed over 2π radians for each value of j and θ. Thus, the *rotational-energy-resolved* anisotropy is given by

$$r_{\hat{\mu}_1\hat{\mu}_2}(j,\theta,t) = (1/2\pi)\int_0^{2\pi} r_{\hat{\mu}_1\hat{\mu}_2}(j,\theta,\psi_0,t)\, d\psi_0 \quad \text{(A-3)}$$

For the case of accidentally symmetric molecules, the transition dipoles may lie along directions not coincident with a principal inertial axis. A large range of practical cases may be covered by allowing $\hat{\mu}_1$ and $\hat{\mu}_2$ to lie anywhere in a plane containing the figure axis, which may be taken as the inertial xz plane without loss of generality. The expression for the

rotational-energy-resolved anisotropy can then be reduced to

$$r_{\mu_{1x}\mu_{1z}\mu_{2x}\mu_{2z}}(j,\theta,t) = {}^1/_{10}({}^1/_2\mu_{1x}{}^2 - \mu_{1z}{}^2)({}^1/_2\mu_{2x}{}^2 - \mu_{2z}{}^2)\cdot\{(3\cos^2\theta - 1)^2 + 12\sin^2\theta\cos^2\theta\cos(j\omega_{no}t) + 3\sin^4\theta\cos(2j\omega_{no}t)\} + \mu_{1x}{}^2\mu_{2x}{}^2\{\cos(2k\omega_{ro}t)({}^9/_{80}\sin^4\theta + {}^3/_{20}(1-\cos^4\theta)\cos(j\omega_{no}t) + {}^3/_{80}(1 + 6\cos^2\theta + \cos^4\theta)\cos(2j\omega_{no}t) - \sin(2k\omega_{ro}t)({}^3/_{10}\cos\theta\sin^2\theta\sin(j\omega_{no}t) + {}^3/_{20}(\cos\theta + \cos^3\theta)\sin(j\omega_{no}t))\} + {}^3/_5\mu_{1x}\mu_{1z}\mu_{2x}\mu_{2z}\{\cos(k\omega_{ro}t)(3\sin^2\theta\cos^2\theta + (2 - \sin^2\theta - 4\sin^2\theta\cos^2\theta)\cos(j\omega_{no}t) + (2\sin^2\theta - \sin^4\theta)\cos(2j\omega_{no}t)) + \sin(k\omega_{ro}t)(2\cos\theta(1 - 2\cos^2\theta)\sin(j\omega_{no}t) - 2\cos\theta\sin^2\theta\sin(2j\omega_{no}t))\} \quad \text{(A-4)}$$

To achieve quantitative agreement with the full quantum treatment at long times, careful consideration must be given to the correspondence between the dimensionless j and k of the classical derivation and the quantum numbers j and k associated with the eigenvalues $j(j+1)\hbar^2$ of the angular momentum squared and $k\hbar$ of the projection of the angular momentum on the molecular figure axis, respectively. In addition to the adjustments mentioned in the text for $j\omega_{no}$ and $2j\omega_{no}$, one must add the replacement of each of the two trigonometric functions of $k\omega_{ro}t$ by an average of the same function of $(k + {}^1/_2)\omega_{ro}t$ and of $(k - {}^1/_2)\omega_{ro}t$.

The observed $r(t)$ requires the ensemble average indicated in eq 2. In the general case of an inhomogeneous population composed of rotationally homogeneous subpopulations fully defined by a set of rotational parameters $\{f\}$, the macroscopic anisotropy is given explicitly by

$$r(t) = \sum_{\{f\}} P_j(\{f\})\, a(\{f\},t)\, r(\{f\},t)/(\sum_{\{f\}} P_j(\{f\})\, a(\{f\},t)) \quad \text{(A-5)}$$

where $P_j(\{f\})$ is the population in state $\{f\}$. The function $a(\{f\},t)$ is the time-dependent amplitude of the isotropic probe signal of the $\{f\}$-state, which is determined by the population dynamics of that state and by the (possibly state-dependent) probe cross sections and detection efficiencies. When the temporal evolution of $a(\{f\},t)$ is common to all probed populations, i.e., $a(\{f\},t) = C(\{f\})\cdot A(t)$ for all $\{f\}$, then the macroscopic anisotropy is strictly determined (in measurements of sufficiently high temporal resolution[15]) by the orientational dynamics of the transition dipoles. Otherwise, $r(t)$ may also reflect population dynamics that simply change the weighting of different $r(\{f\},t)$'s in the average in eq A-5.

Acknowledgment. This research was supported by the National Science Foundation and Air Force Office of Scientific Research.

References and Notes

(1) Pauling, L. *The Nature of the Chemical Bond and the Structure of Molecules and Crystals*; Cornell University Press: Ithaca, NY, 1940 (see also references therein).

(2) Debye, P. *Polar Molecules*; Chemical Catalog Company: New York, 1929.

(3) Perrin, F. *J. Phys. Radium* **1934**, *5*, 497−511; **1936**, *7*, 1.

(4) Chuang, T. J.; Eisenthal, K. B. *J. Chem. Phys.* **1972**, *57*, 5094. Eisenthal, K. B. *Acc. Chem. Res.* **1975**, *8*, 118 and references therein.

(5) Steele, W. A. *J. Chem. Phys.* **1962**, *38*, 2404, 2411.

(6) Gordon, R. G. *J. Chem. Phys.* **1966**, *44*, 1830.

(7) Felker, P. M.; Zewail, A. H. Molecular Structure from Ultrafast Coherence Spectroscopy. In *Femtosecond Chemistry*; Manz, J., Wöste, L., Eds.; VCH Publishing: New York, 1994; Vol. I, pp 193−260 (see also references therein).

(8) Baskin, J. S.; Zewail, A. H. *J. Phys. Chem.* **1994**, *98*, 3337.

(9) Felker, P. M. *J. Phys. Chem.* **1992**, *96*, 7844.

(10) Negus, D. K.; Green, D. S.; Hochstrasser, R. M. *Chem. Phys. Lett.* **1985**, *117*, 409. Meyers, A. B.; Holt, P. L.; Pereira, M. A.; Hochstrasser, R. M. *Chem. Phys. Lett.* **1986**, *132*, 585.

(11) Scherer, N. F.; Shepanski, J. F.; Zewail, A. H. *J. Chem. Phys.* **1984**, *81*, 2181. Scherer, N. F.; Khundkar, L.; Rose, T. S.; Zewail, A. H. *J. Phys. Chem.* **1987**, *91*, 6478.

(12) Borisevich, N. A.; Khoroshilov, E. V.; Kryukov, I. V.; Kryukov, P. G.; Shirkov, A. V.; Blokhin, A. P.; Tolstorozhev, G. B. *Chem. Phys. Lett.* **1992**, *191*, 225.

(13) Baskin, J. S.; Chachisvilis, M.; Gupta, M.; Zewail, A. H. *J. Phys. Chem. A* **1998**, *102*, 4158. Baskin, J. S.; Gupta, M.; Chachisvilis, M.; Zewail, A. H. *Chem. Phys. Lett.* **1997**, *275*, 437.

(14) Felker, P. M.; Zewail, A. H. *J. Chem. Phys.* **1987**, *86*, 2460. Felker, P. M.; Baskin, J. S.; Zewail, A. H. *J. Phys. Chem.* **1986**, *90*, 724.

(15) Baskin, J. S.; Felker, P. M.; Zewail, A. H. *J. Chem. Phys.* **1987**, *86*, 2483.

(16) Herzberg, G. *Molecular Spectra and Molecular Structure*; Van Nostrand Reinhold: New York, 1945; Vol. II, p 23.

(17) Baskin, J. S.; Zewail, A. H. *J. Phys. Chem.* **1989**, *93*, 5701.

(18) Williams, R. M.; Papanikolas, J. M.; Rathje, J.; Leone, S. R. *Chem. Phys. Lett.* **1996**, *261*, 405.

(19) Zewail, A. H. *J. Chem. Soc., Faraday Trans. 2* **1989**, *85*, 1221.

(20) Felker, P. M.; Zewail, A. H. Rotational Coherence Phenomena. In *Jet Spectroscopy and Molecular Dynamics*; Hollas, J. M., Phillips, D., Eds.; Blackie Academic and Professional: Glasgow, 1995; pp 181−221 (the reader is advised to be aware of publisher's errors in some sections); and references therein.

(21) See, e.g.: Blokhin, A. P.; Gelin, M. F.; Dreier, T. *Phys. Chem. Chem. Phys.*, **1999**, *1*, 5583. Frey, H.-M.; Beaud, P.; Gerber, T.; Mischler, B.; Radi, P. P.; Tzannis, A. P. *Appl Phys B−Lasers O* **1999**, *68*, 735.

(22) Edwardes, E. *Q. J. Pure Appl. Math* **1892**, *26*, 70.

(23) Hansen, J. P.; McDonald, I. R. *Theory of simple liquids*, 2nd ed.; Academic Press: London, 1986. Coffey, W. T.; Kalmykov, Y. P.; Waldron, J. T. *The Langevin Equation*; World Scientific: Singapore, 1996.

(24) Hu, C.-M.; Zwanzig, R. *J. Chem. Phys.* **1974**, *60*, 4354.

(25) Gelin, M. F. *J. Phys. Chem. A* **2000**, *104*, 6150.

(26) Sension, R. J.; Hochstrasser,R. M. *J. Chem. Phys.* **1993**, *98*, 2940. Youngren, G. K.; Acrivos, A. *J. Chem. Phys.* **1975**, *63*, 3846.

(27) Waldeck, D. H. The Role of Solute−Solvent Friction in Large-Amplitude Motions. In *Conformational Analysis of Molecules in Excited States*; Waluk, J., Ed.; Wiley-VCH: New York, 2000; pp 113−176 (see also references therein).

(28) Zhong, D.; Douhal, A.; Zewail, A. H. *Proc. Natl. Acad. Sci. U.S.A.* **2000**, *97*, 14056.

(29) Baskin, J. S.; Semmes, D. H.; Zewail, A. H. *J. Chem. Phys.* **1986**, *85*, 7488.

(30) Dantus, M.; Bowman, R. M.; Baskin, J. S.; Zewail, A. H. *Chem. Phys. Lett.* **1989**, *159*, 406.

(31) Semmes, D. H.; Baskin, J. S.; Zewail, A. H. *J. Am. Chem. Soc.* **1987**, *109*, 4104.

(32) Semmes, D. H.; Baskin, J. S.; Zewail, A. H. *J. Chem. Phys.* **1990**, *92*, 3359.

(33) Volk, M.; Gnanakaran, S.; Gooding, E.; Kholodenko, Y.; Pugliano, N.; Hochstrasser, R. M. *J. Phys. Chem. A* **1997**, *101*, 638.

(34) Bürsing, H.; Vöhringer, P. *Phys. Chem. Chem. Phys.* **2000**, *2*, 73.

(35) See, *e. g.*, Pauling, L.; Wilson, E. B. *Introduction to quantum mechanics, with applications to chemistry*; McGraw-Hill: New York, 1935.

(36) See, *e. g.*, Cross, P. C.; Hainer, R. M.; King, G. W. *J. Chem. Phys.* **1944**, *12*, 210.

(37) Felker, P. M.; Zewail, A. H. Ultrafast dynamics of IVR in molecules and reactions. In *Jet Spectroscopy and Molecular Dynamics*; Hollas, J. M., Phillips, D., Eds.; Blackie Academic and Professional: Glasgow, 1995; pp 222−308 (the reader is advised to be aware of publisher's errors in some sections).

(38) Arasaki, Y.; Takatsuka, K.; Wang, K.; McKoy, V. *J. Chem. Phys.* **2000**, *112*, 8871 and references therein for earlier work.